Journal Pre-proof

Water flow decrease of track-etched polyethylene terephthalate membranes

Ana Ambrož, Zhen Yao, Christopher Rojas, Polina Angelova, Armin Gölzhäuser, Irena Petrinić

PII: S0376-7388(25)00607-6

DOI: https://doi.org/10.1016/j.memsci.2025.124294

Reference: MEMSCI 124294

To appear in: *Journal of Membrane Science*

Received Date: 24 March 2025

Revised Date: 23 May 2025

Accepted Date: 1 June 2025

Please cite this article as: A. Ambrož, Z. Yao, C. Rojas, P. Angelova, A. Gölzhäuser, I. Petrinić, Water flow decrease of track-etched polyethylene terephthalate membranes, *Journal of Membrane Science*, https://doi.org/10.1016/j.memsci.2025.124294.

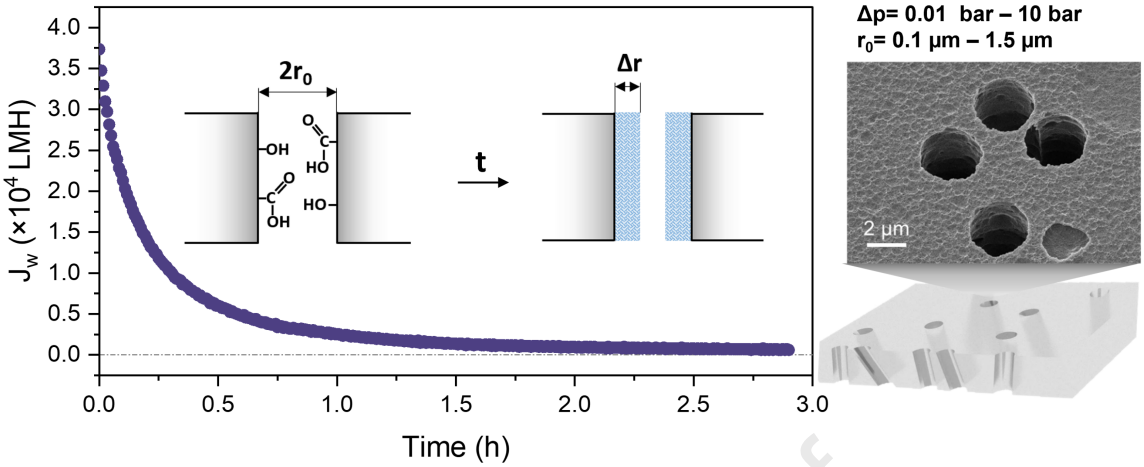

Water flow decrease of track-etched polyethylene terephthalate membranes

Ana Ambrož[a,b], Zhen Yao[b*], Christopher Rojas[c], Polina Angelova[b], Armin Gölzhäuser[b], Irena Petrinić[a]

[a] *University of Maribor, Faculty of Chemistry and Chemical Engineering, Smetanova ulica 17, 2000 Maribor, Slovenia*

[b] *Bielefeld University, Faculty of Physics, Universitaetsstrasse 25, 33615 Bielefeld, Germany*

[c] *CNM Technologies GmbH, Blomestrasse 10, 33609 Bielefeld, Germany*

**zhen.yao@uni-bielefeld.de*

Abstract

Track-etched polyethylene terephthalate (TE-PET) membranes, characterized by their well-defined cylindrical pores and narrow pore size distribution, offer advantages in filtration applications but demonstrate a gradual decrease of water flux over time. In this work, we evaluate the performance of track-etched polyethylene terephthalate (TE-PET) membranes as microfilters in low-pressure cross-flow and dead-end filtration systems. Membranes with pore sizes between 0.2 and 2.5 µm and porosities of 0.2–20% were tested at different low pressures (0.02–10 bar). Monitoring water flux over time exhibited a significant reduction. This behaviour is attributed to polymer swelling within the pore walls due to the formation of a sol-gel film. Notably, this swelling is enhanced under dynamic flow conditions, with larger pores exhibiting more rapid and pronounced flux decline. When filtering organic solvents, the flux drop is less pronounced and depends on their viscosity and polarity. Surface characterization by atomic force microscopy further confirmed morphological changes in TE-PET support after water filtration. Additional contributing factors, such as fouling and compaction, are also discussed.

Keywords: Track-etched support; Polyethylene terephthalate; Water filtration; Swelling; Sol-gel Film; Carbon nanomembrane.

1. Introduction

Track-etched (TE) membranes represent a unique class of filtration materials, consisting of perforated polymer foils with straight pores ranging from 0.001–10 µm in diameter and 5–50 µm in thickness[1,2]. These membranes are fabricated through a two-step process: First, polymer films are irradiated with heavy ions with kinetic energies of several hundred megaelectron volts, creating linear ion tracks where polymer covalent bonds are broken. Subsequently, chemical etching selectively removes material much faster from these damaged zones than from the bulk, forming cylindrical pores[3]. The resulting membranes exhibit precisely controlled pore sizes with densities varying between 1 and 10^{10} cm^{-2}. The final pore size and shape are determined by the etching conditions. Despite their structural precision, TE membranes typically exhibit low porosity (often below 30%), that can limit their applicability in high-throughput filtration. Increasing pore density to compensate may lead to the formation of multiplets, coincidental pore intersections at the surface that can influence local flux distribution, reduce solute rejection, and elevate the risk of fouling[4]. To minimize multiplet formation, multi-angle ion irradiation can be employed.

Three polymers have emerged as dominant in TE membrane fabrication due to their high etch ratios (the ratio between track etch rate and bulk etch rate): polycarbonate (PC)[5],[6–10] polyimide (PI)[11,12] and polyethylene terephthalate (PET)[13–16].

Compared to conventional membranes, TE membranes offer distinct advantages through their narrow pore size distribution and pore geometry. However, their relatively high production costs have limited their implementation into small and mobile devices for specialized uses, such as highly sensitive and fast bacterial filters in food, cosmetic and pharmaceutical industries, control barriers in glucose sensors in point-of-care devices[17], and selective biomolecule barriers in medical implants[18]. Beyond these, TE membranes can potentially be used as optical sensors[19] and biosensors[20,21] for different analytes in clinical specimens. They are also studied in diverse separation processes, including gas separation[22], water–oil emulsion separation[23,24], as separators in lithium batteries[25,26], and in pharmaceutical separation processes[27]. Previous studies also examined them as substrates for thin-film composites (TFCs) covered by polyamide skin layer formed through interfacial polymerization[5,28–32]. The development of next-generation TFC reverse osmosis (RO) and forward osmosis (FO) membranes has highlighted the limitations of conventional thick, 3D porous substrates, which restrict water flux and cause significant internal concentration polarization. Consequently, recent research has focused on reducing substrate thickness or developing alternative support structures. In this context, PET TE polymer foils present a promising platform due to their excellent chemical resistance, small thickness and good mechanical stability[17].

Despite these advantages, the application of TE-PET as a support in TFC membranes has not been thoroughly evaluated so far. Some early work has reported water flux reduction over time[33,34], with one noting a 65% decrease in water flux for TE-PET (0.2 µm pores, 9.4% porosity) under 0.34 bar over a 3-hour period[35]. Similar decline has been also observed in TE-PC membranes,

where a 4-11% flux decline occurred within 25 minutes for membranes with 1 µm pores and 15.7% porosity at pressures between 2.5 and 7.5 mbar [36]. Other studies have noted even higher declines in water flux, often attributing the flux reduction to fouling [37], which is influenced by factors such as protein concentration and pore size [38]. These findings suggest that flux decline is a broad issue among TE membranes, yet its underlying mechanisms and influencing factors remain poorly understood and require systematic investigation.

In this work, we present a comprehensive study of the flow decline in TE-PET as a function of time, pore sizes, and porosity, utilizing both in-house etched and commercially obtained membranes. The filtration was conducted at a wide overpressure range (0.01–10 bar), aiming to mimic the conditions in the devices in which they are or will potentially be implemented[17]. We monitored water flow across TE-PET membranes by multiple or long-term filtrations. In addition to pristine TE-PETs, we tested one TFC membrane using TE-PET as support. Our study reveals that the primary cause of flux downturn is the swelling of a sol-gel film formed on the pore walls during chemical etching[39]. The swelling progressively reduces effective pore sizes, resulting in a drop of water flow and altered membrane performance.

2. Materials and Methods

2.1 TE-PET samples

Commercially available TE-PET films were obtained from it4ip S.A., Ottignies-Louvain-la-Neuve, Belgium. In-house etched PET films were prepared by CNM Technologies GmbH, Bielefeld, Germany, from ion-beamed films TRAKETCH® obtained from SABEU GmbH & Co. KG, Northeim, Germany, with thicknesses of 23-36 µm and ion densities from 6×10^5 to 1.5×10^7 ions/cm^2. The latent pores were opened by floating over 5 M sodium hydroxide solution at 80°C. By varying the etching time and initial pore density of the PET foil, pore sizes between 0.5-4.0 µm were achieved.

2.2 Chemicals and solvents

All chemicals used were of analytical grade unless otherwise specified. The following solvents were used for comparative filtration studies: ultrapure water (resistivity 18.2 MΩ·cm, TOC < 200 ppb, MiliPore), n-hexane (min. 99.0%, Chemsolute), 2-propanol (AnalaR NORMAPUR, VWR Chemicals), and ethanol (≥ 99.8%, Thermo Fisher Scientific). These solvents represent a range of polarities, dipole moments, and hydrogen bonding capabilities (see Table 1).

Table 1: Physical and chemical properties of solvents used in TE-PET membranes testing.

Solvent	**n-hexane**	**2-propanol**	**ethanol**	**water**
Formula	C_6H_{14}	C_3H_8O	C_2H_6O	H_2O
M_W (g/mol)	86.17	60.10	46.07	18.01
Viscosity at 20°C (mPas)[40]	0.324	2.37	1.2	0.89
Density at 20°C (g/L)[40]	660	781	789	998.3
Kinetic diameter at 20°C (nm)[41–43]	~0.43	~0.47	~0.45	~0.30
Polarity index[44]	0.0	4.3	5.2	9.0
Dipole moment (D)[44,45]	0.0	1.66	1.73	1.82

2.3 Composite membranes

TFC-composite membranes using TE-PETs as supports were supplied by CNM Technologies GmbH, Bielefeld, Germany. These membranes, from here on referred to as CNM-composites, are prepared directly on ion-bombarded PET substrates according to a transfer-free procedure and have conical pores in TE-PET supports[46]. The tested sample is 36 µm thick with pore sizes of 2 µm, and 0.3% areal porosity. Areal porosity corresponds to the active surface area of the skin layer.

2.4 Methods

Dead-end filtration experiments were conducted using a home-built filtration setup equipped with a 70 mL filtration cell with an effective membrane area of 0.07 cm² (Figure S1b). Compressed nitrogen was used to maintain the required pressure gradient across the membrane. TE-PET samples with pore sizes of 0.2 µm, 0.4 µm, 0.8 µm, and 2.5 µm were tested under various applied pressures (detailed in Table 2) using ultrapure water (resistivity 18.2 MΩ·cm, TOC < 200 ppb) as the feed solution. Permeate mass was continuously measured using a precision balance, with the data automatically recorded in computer software. Water flux was calculated using

$$J = \frac{\Delta m/\rho}{A \cdot \Delta t} \quad (1)$$

where Δm is the mass of the permeate, ρ is the density of the permeate, A is the effective area of the membrane, and Δt is the time. The permeability P is then given by

$$P = \frac{J}{\Delta p} \quad (2)$$

where Δp is the transmembrane pressure applied.

All experiments were conducted at 20 ± 1°C with relative humidity maintained at 50 ± 5%. Each measurement was repeated at least two times to ensure reproducibility.

A low-pressure reverse osmosis (LPRO) cross-flow setup was also employed to evaluate the intrinsic water permeability of the TE-PET membrane and the separation performance of CNM-composites. The system utilized a laboratory cross-flow cell with an effective membrane area of 12.4 cm^2 (Figure S1a). Ultrapure water was used as a feed solution for TE-PET membranes. For CNM-composites, both ultrapure water and 1 g/L sodium chloride (NaCl) were used as feed solutions. Permeate mass was continuously monitored by a digital balance (Scout PRO 4000g, OHAUS, New Jersey, USA). The water flux and permeability were calculated using Eq. 1 and Eq. 2, respectively. The separation efficiency of NaCl was evaluated by calculating the rejection R (%) using[47]

$$R = \left(1 - \frac{C_p}{C_f}\right) \cdot 100\% \quad (3)$$

where c_p is the NaCl concentration in the permeate, and c_f is the NaCl concentration in the feed solution. All experiments were conducted at 23 ± 1°C.

Low pressure flux measurements with water reservoir were carried out using a home-built polycarbonate cell with 3 cm^2 active membrane area (Figure S1c). The trans-membrane pressure was generated by positioning a water reservoir approximately 20 cm above the membrane, corresponding to an initial hydrostatic pressure of ~0.02 bar. The reservoir had a large cross-sectional area (33 cm^2), which limited the drop in water level during filtration. Flux was determined based on the time required for 50 mL of water to pass through the membrane. This volume corresponds to a water level decrease of approximately 1.5 cm, resulting in a pressure change of ~0.0015 bar (7.5% of the initial pressure). Due to the small magnitude of this change, the pressure was considered effectively constant for the purpose of flux calculations.

2.5 Membrane characterization

Helium Ion Microscopy (HIM) images were acquired with a Carl Zeiss Orion Plus instrument (ZEISS, Oberkochen, Germany) with a He^+ beam energy of 33.5 kV and a beam current of ~0.1 pA. An electron flood gun was used to compensate the charging effects.

Optical microscopic images were made by Olympus BX51 (Olympus Corporation, Tokyo, Japan). Atomic force microscopy (AFM) was performed by NT-MDT, Ntegra, Apeldoorn, Netherlands in tapping-mode, utilizing a Tap300Al-G probe (Budget Sensors, Sofia, Bulgaria, k ≈ 40 N m^{-1}, f_0 ≈ 300 kHz) under ambient conditions.

IR measurements were conducted on FT-IR spectrometer Vertex 70 (Bruker, Massachusetts, USA) with attenuated total reflection (ATR) accessory. Spectra were recorded in the range of 4500 cm^{-1} to 600 cm^{-1} with a resolution of 4 cm^{-1} and an average of 16 scans.

Total organic carbon (TOC) content was analyzed using a Multiwin 3100 TOC/TNb analyzer (Analytic Jena GmbH, Jena, Germany), employing the non-purgeable organic carbon (NPOC) method. The samples were adjusted to pH < 2 by acidification with HCl (2 M, Merck, Darmstadt, Germany) and purged with oxygen to remove total inorganic content.

3. Results and discussion

3.1 Initial membrane characteristics

TE-PET membranes with well-defined cylindrical pores were prepared through heavy ion bombardment followed by chemical etching[1,2]. Figure 1a shows a schematic and representative HIM image of the membrane structure, showing uniform pore distribution with precise diameter control. As expected from their straight and uniform channels, TE-PETs exhibit exceptionally high water permeability[48]. To systematically investigate its behaviour in water filtration applications, we evaluated various TE-PET membranes with pore sizes ranging from 0.2 µm to 2.5 µm and ion

densities from 4×10^5 ions/cm^2 to 5×10^8 ions/cm^2, resulting in membrane porosities between 0.2% and 20%, as detailed in Table 2.

The initial pure water transport properties of these membranes align well with theoretical predictions. Figure 1b shows the water permeability per pore as a function of pore size, following the Hagen-Poiseuille equation modified to account for potential slip effects:

$$P_{HP+slip} = \frac{\pi r^4}{8\eta L}\left(1 + \frac{4b}{r}\right) \quad (4)$$

where r is the pore radius, η is the fluid dynamic viscosity, L is the channel length (approximated by membrane thickness), and b is the slip length (that varies from 0 to 0.2 µm in our analysis). This agreement confirms the initial structural integrity and uniform pore geometry of the membranes.

Table 2: Properties and filtration methods of tested TE-PET membranes.

Pore size (top/bottom)* / µm	**ion density / cm^{-2}**	**Porosity / %**	**Pore shape**	**Method of pressure applied**	**Water permeability / L m^{-2} h^{-1} bar^{-1}**	**Water permeability per pore / L h^{-1} bar^{-1}**
0.2	5×10^8	15.7	cylindrical	water reservoir 20 cm above the membrane	5132	1.02×10^{-9}
0.7	3×10^7	11.6			34041	1.13×10^{-7}
0.8	4×10^7	20.1			60895	1.52×10^{-7}
1.8	6×10^5	1.5			100124	6.67×10^{-6}
0.75/1.1	1.5×10^7	6.6	conical		45773	3.05×10^{-7}
1.5/2.3	6×10^5	1.1			10532	1.75×10^{-6}
2.5/2.9	6×10^5	3.0			138315	2.31×10^{-5}
1	4×10^5	0.3	cylindrical	pressurized N_2 (0.5-10 bar) cross-flow	265	6.63×10^{-8}
0.7/2.0	6×10^5	0.2	conical		629	1.05×10^{-7}
1/1.5	6×10^5	0.5			772	1.38×10^{-7}
1.1/1.6	2×10^6	1.9			7320	3.66×10^{-7}
0.2	5×10^8	15.7	cylindrical	pressurized N_2	11287	2.86×10^{-9}
0.4	1.5×10^8	18.9			29801	1.99×10^{-8}

0.8	4×10^{7}	20.1		(0.5-2 bar) dead-end	175337	4.57×10^{-7}
2.5	3×10^{6}	14.6			560788	2.07×10^{-5}

* Pore sizes were determined via optical microscopy and high-resolution imaging techniques (HIM/AFM). For conical pore geometries, the top and bottom pore sizes represent diameter measurements obtained from the entry and exit faces of the membrane, respectively.

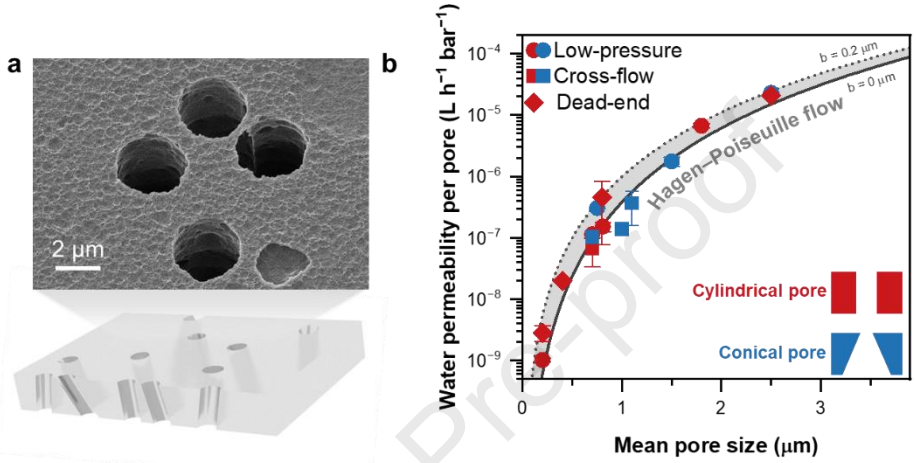

Figure 1. (a) Schematic and exemplary HIM image of track-etched PET membranes with pore diameter of 2 µm. (b) Measured water permeability per single pore as a function of the mean pore size. The shaded region represents the theoretical trend predicted by the Hagen-Poiseuille equation, considering a slip length range of 0 µm (full line) to 0.2 µm (dotted line).

As fabricated from high-energy ion bombardment followed by chemical etch[21], the formation of PET pores goes through fast track core etching, swelling of the penumbra (region, surrounding the core, containing smaller polymer fragments) and dissolution of the formed gel[49]. The etching process introduces significant surface functionality to the membrane. The pore walls contain carboxyl and hydroxyl groups resulting from hydrolyzation of ester bonds during chemical etching[50–52]. These hydrophilic moieties lead to isoelectric points between 2.3 and 3 (Figure S3), slightly lower than literature values of 3.8[53]. The surface charge densities in ultrapure water at pH ~6.5, as calculated from the Grahame equation[54,55], vary from -3×10^{-3} to -8×10^{-3} C/m^2, corresponding to < 1 carboxyl groups per 10 nm^2 (see Table S1). These charged groups create localized hydrophilic regions within the otherwise hydrophobic PET matrix. The formation of carboxyl and hydroxyl groups during alkaline etching is further confirmed by FTIR analysis of the pristine TE-PET membranes (see S4 in SI for details), which shows a weak band at 3423 cm^{-1} corresponding to O-H stretching of alcohols[52]. Adjacent to the intensive C=O stretching of ester carboxyl groups, there is a shoulder peak at 1685 cm^{-1}, which is attributed to

197 the C=O stretching of carboxylic acid groups, potentially formed during hydrolysis and bonded to
198 the aromatic group.

199 **3.2 Dynamic water transport behaviour**

200 Despite their well-defined initial structure, TE-PET membranes exhibit significant changes in water
201 transport properties during operation. Dead-end filtration experiments on TE-PETs with various
202 pore sizes revealed consistent patterns of flux decline across various operating conditions
203 (Figure 2a). The reduction in water flux follows similar trends for membranes with different pore
204 sizes (0.2-0.8 µm) and remains consistent across the applied pressure range (0.5-2 bar). Flux
205 decline is associated with effective pore size reduction. Two potential mechanisms for pore size
206 reduction can be excluded here: First, mechanical compression is ruled out as the relative flux
207 reduction remained consistent throughout the applied pressure range (0.5–2 bar, see also
208 Figure S5 for the membrane cross-section before and after filtration). Second, bulk material
209 behaviour cannot account for the pore size reduction, as PET is inherently hydrophobic with
210 minimal water absorption (less than 1% g/g_{DRY})[56,57] and limited bulk expansion (~2% [58]). The
211 observed water flux reduction exceeding 20% thus points to phenomena specifically occurring
212 within the pore structure rather than bulk material properties.

213 The mechanism underlying these changes appears to originate from the chemical structure
214 created during pore formation. The track etching process proceeds through sequential stages: fast
215 track core etching, penumbra swelling, and dissolution of the formed gel[49]. This process leaves
216 residual cross-linked structures on the pore walls, containing carboxyl and hydroxyl
217 groups[50,51,59,60]. Under filtration, these highly hydrophilic moieties facilitate water absorption
218 through hydrogen bonds, creating gel again and causing volumetric expansion[39]. This inward
219 swelling, as illustrated schematically in Figure 2b, effectively reduces the available space for fluid
220 flow through the pore and therefore gives rise to a reduced flux.

221 The rapid decrease in flux is observed exclusively during filtration, i.e., under dynamic flow
222 condition. Even a small pressure of 0.02 bar, generated by a water reservoir positioned 20 cm
223 above the membrane, results in a significant flux reduction of over 20% within an hour (as shown
224 in Figure S1c). Long term cross-flow measurements on low porosity (0.3-2%) membranes further
225 reveal fluxes decline to nearly 0 LMH after 3h (Figurec and Figure S1a). In contrast, under static
226 conditions, e.g., 2h pre-immersion in water or 2h soaking under hydraulic pressure within the cell,
227 the initial flux decreases by < 10%, which is within the margin of error and noticeably smaller than
228 the reduction observed during 300 s of filtration at 0.5 bar. Over time, the flux change for soaked
229 samples remains consistent with that of pristine samples, suggesting similar swelling behaviour.
230 Extending the soaking duration to 39 hours does not result in further reduction in the initial flux
231 and exhibits very similar swelling behaviour (Figured). Pressure-pause experiments further
232 confirmed the persistence of the reduced permeability after pressure removal and reapplication,
233 ruling out reversible phenomena (see S2 in SI for details). These results suggest that swelling takes

place faster under flow conditions than in static water. The swelling effect shows strong dependence on pore size. Larger pores (2.5 µm) demonstrated more pronounced and faster reductions in flux, reaching 80% of the initial flux within 70 s, compared to 200 s for 0.8 µm pores and 1200 s for 0.2 µm pores (Figuree).

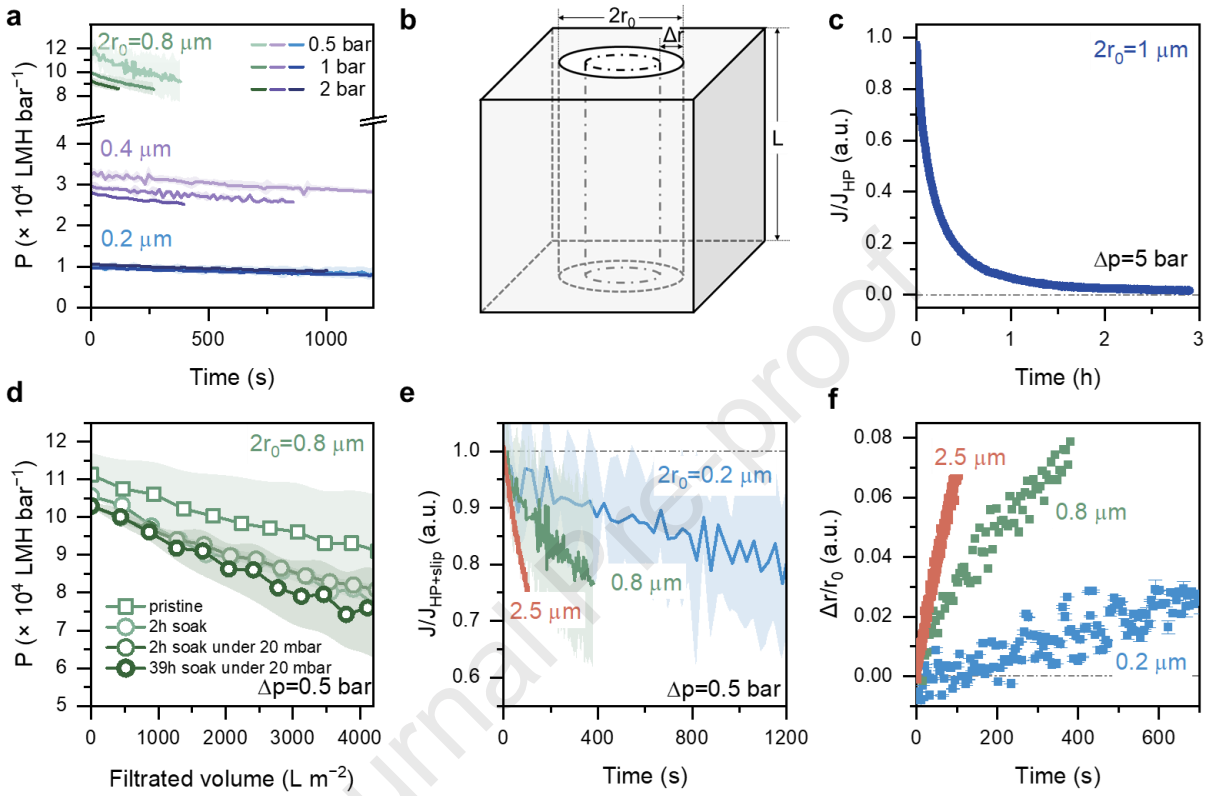

Figure 2. (a) Water permeability as a function of time for TE-PET with 0.2 µm (15.7% porosity), 0.4 µm (18.9%) and 0.8 µm (20.1%) pores at different applied pressures. (b) Schematic illustration of the pore size reduction during filtration. (c) Long-term cross-flow water filtration at 5 bar for TE-PET with 1 µm pores and 0.3% porosity. (d) Water permeability as a function of filtrated volume for TE-PET (0.8 µm pores and 20.1% porosity) soaked in water prior to the filtration measurements. (e) Normalized water fluxes and (f) relative pore radius changes as a function of filtration time for TE-PETs at 0.5 bar with pore sizes of 0.2 µm, 0.8 µm and 2.5 µm (14.6% porosity). The shaded area in (a), (d), (e) represents the standard deviation, based on measurements from at least two independent samples.

The observed flux reduction can be quantitatively analysed using the Hagen-Poiseuille equation under negligible slip condition relating the change in effective pore radius (Δr) to the measured flux (J):

$$\Delta r = r_0 - r_t = r_0[1 - (J/J_{HP+slip})^{1/4}] \quad (5)$$

where r_0 and r_t re the initial and time-dependent pore radii, respectively, and $J_{HP+slip}$ is Hagen-Poiseuille flux accounting for potential slip effects.

The corresponding volumetric change in the pore structure, denoted as V_{swell}, follows:

$$V_{swell} = \pi L(r_0{}^2 - r_t{}^2) \quad (6)$$

As illustrated in Figuref and Figure 3, larger pores exhibited greater relative radius changes ($\Delta r/r_0$) and volumetric changes, suggesting them to be more susceptible to dynamic swelling under flow conditions. Plotting flux against filtrated volume (Figure S6) further confirms this dynamic effect, with flux continuously declines with volume filtered, with larger pores showing steeper reductions. Larger pores have a lower length-to-radius ratio (L/r), which makes them mechanically less stable and more prone to deformation during swelling[61]. Additionally, their larger surface area ($\propto L \cdot r$) enhances interaction with water, promoting faster swelling.

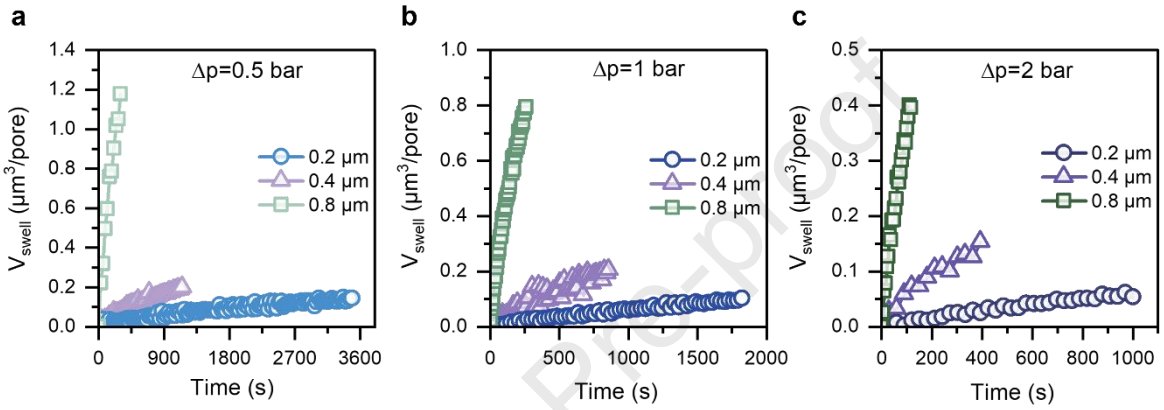

Figure 3. Swelling volume per pore of TE-PET membranes as a function of filtration time for different pore sizes 0.2 μm (15.7% porosity), 0.4 μm (18.9%) and 0.8 μm (20.1%) at (a) 0.5 bar, (b) 1 bar, and (c) 2 bar.

3.3 Surface morphology evolution

To investigate the structural changes of the pore during swelling, we followed the surface morphologies of TE-PET as a function of filtration time. While optical microscopy showed minimal visible changes, AFM measurements revealed significant progressive changes in pore dimensions and morphology (Figure 4a). The height profiles clearly illustrate the swelling process, with initial pore depressions gradually filling in over time. After 48 hours of water filtration, pore depth decreased significantly, and by 144 hours, further reduction occurred with some pores completely sealed, forming protrusions hundreds of nanometers in height. Notably, neighbouring surface features unrelated to pores (highlighted by the grey area in Figure 4a) maintained constant profiles, confirming that the swelling phenomenon is localized specifically to pore regions.

The track etching process leaves a high concentration of oligomers resides within the pores. Upon water passage part of them are rinsed and extruded from the pores. Our experiments confirm that dynamic flow conditions enhance the removal of these oligomers compared to static conditions. While soaking TE-PET in water for 1 hour increased the TOC from 200 μg/L to 467 μg/L, filtration at 0.5, 1, and 1.5 bar produced even higher TOC values of 592, 802, and 766 μg/L, respectively. The slight decrease at 1.5 bar suggests that the extractable species become depleted

after the initial filtration steps (detailed results in SI S7). Despite this measurable extraction of oligomers, the majority of oligomers appear to remain within the polymer structure, contributing to the observed pore closure. Figure 4b and 4c provide further visual evidence, showing dried gel layer accumulated inside a 1 µm and 2.5 µm pore under cross-flow and dead-end filtration conditions, respectively.

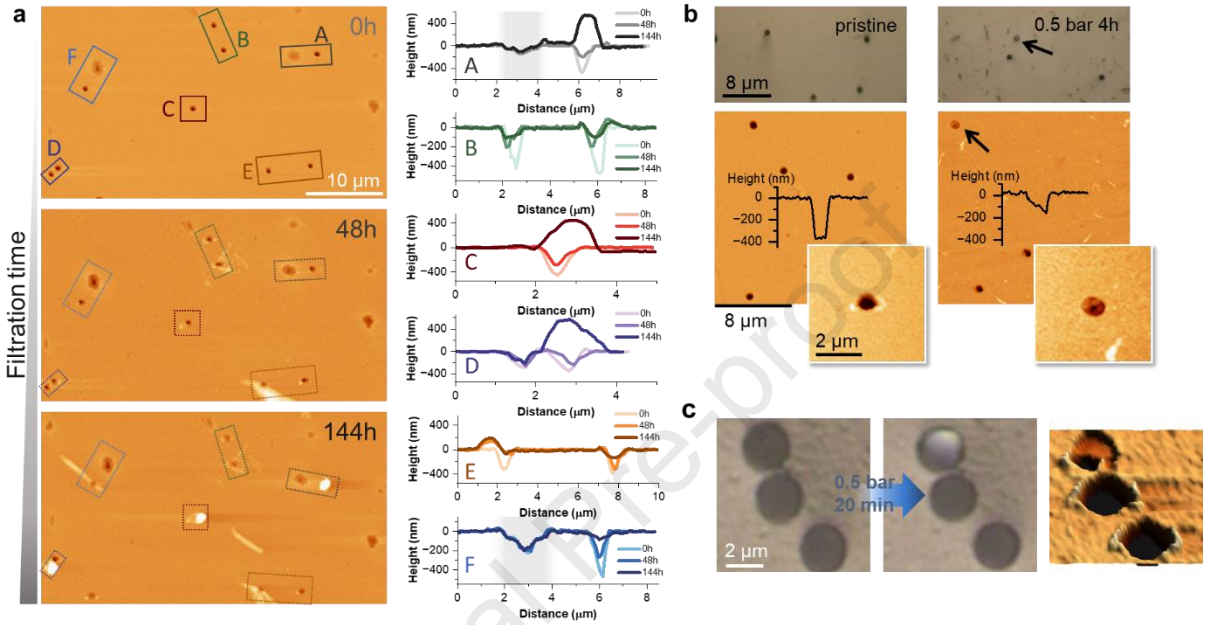

Figure 4. (a) AFM images of TE-PET with 1 µm pores (0.31% porosity) at 10 mbar after 0 h, 48 h and 144 hours filtration with A-F showing the height profiles of corresponding regions marked. The gray areas mark the unchanged surface features. (b) Comparison of optical microscope, AFM images and height profiles of the pristine TE-PET (1 µm pore, 0.31% porosity) and after 4 h filtration at 0.5 bar under cross-flow condition. The arrows mark the clogged pores with visible gel formation. (c) Optical images (left and middle) of TE-PET with 2.5 µm pores (14.6% porosity) before and after 20 min dead-end filtration at 0.5 bar and AFM image (on the right) after 20 min filtration showing accumulated gel layer within pores.

The membrane thickness of approximately 23 µm means that surface observations may not always capture the full extent of internal swelling. For instance, in membranes with 2.5 µm pores, calculations predict a 13% reduction in effective radius after 20 minutes of water filtration at 0.5 bar. However, optical images and AFM measurements reveal exclusion of gel and clogging in only 3-6% of the pores, suggesting that significant changes occur within the pore channel that may not be immediately apparent at the surface. This fraction was estimated by analyzing optical images over multiple representative membrane areas (Figure S8).

3.4 Solvent effects on membrane performance

The profound swelling of TE-pores in water significantly limits its application in aqueous medium. Since the penetration of liquid into a polymer is dependent on the interaction between the solvent and the polymer[62], to mitigate the swelling, we investigated membrane performance using a

range of solvents with different chemical properties, including polar alcohols and non-polar organic solvents. The permeability of TE-PET membranes is strongly influenced by solvent viscosity and interactions at the membrane interface. As shown in Figure 5a, the initial solvent flux (J_0) decreases with increasing viscosity (η), following the expected trend described by the Hagen-Poiseuille equation for slip lengths ranging from 0.025 to 0.062 µm.

Comparative filtration experiments with different solvents (Figure 5b) revealed that membrane performance is not solely determined by viscosity but is strongly influenced by specific solvent-membrane interactions. Water, with its high dipole moment (1.82 D) and strong hydrogen bonding capability, induced the most significant flux decline and swelling. Ethanol and 2-propanol, though still polar, exhibited moderate swelling due to their larger molecular sizes, lower dipole moments, and reduced hydrogen bonding potential. In contrast, n-hexane, being nonpolar and interacting only via weak van der Waals forces, resulted in minimal flux decline and negligible swelling.

These findings demonstrate that the advantageous structural properties of TE-PET membranes can be effectively applied in filtration applications by careful selection of operating conditions and solvents that minimize swelling effects.

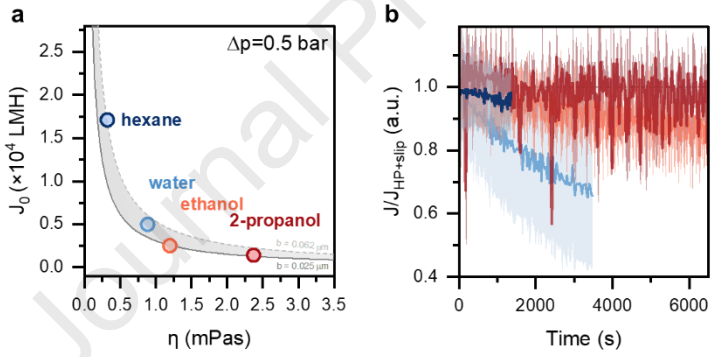

Figure 5. (a) Initial solvent flux (J_0) as a function of viscosity (η) for different solvents for TE-PET with 0.2 µm (15.7% porosity). The shaded region represents the theoretical trend predicted by the Hagen-Poiseuille equation, considering a slip length range of 0.025 µm (full line) to 0.062 µm (dotted line). (b) Normalized flux as a function of filtration time for different solvents.

3.5 Fouling vs. Swelling

To differentiate between fouling and swelling effects, comparative experiments were conducted using fresh ultrapure water and aged water (stored in plastic bottles for 4 months). FTIR spectroscopy revealed distinct differences between pristine membranes and those tested with fresh and aged water (Figure 6a). Membranes tested with aged water showed characteristic bands at 2848 cm^{-1} and 2916 cm^{-1}, corresponding to CH_2 symmetric and asymmetric stretching vibrations of long-chain hydrocarbons. Additionally, the presence of an amide II band at 1540 cm^{-1}

(N-H bending and C-N stretching vibrations) indicates protein-based fouling. These characteristic bands are absent in both pristine membranes and those tested with fresh water, confirming that organic fouling occurs primarily with aged water samples.

Optical microscopy analysis of post-filtration membranes provided further evidence of fouling mechanisms. Membranes exposed to aged water exhibited visible debris accumulation on the surface (Figure 6b), contributing to additional resistance to water transport. This increased resistance leads to more rapid flux decline compared to fresh water filtration, as demonstrated by the water flux measurements of the TE-PET membrane with 0.8 µm pore diameter at 0.5 bar (Figure 6c).

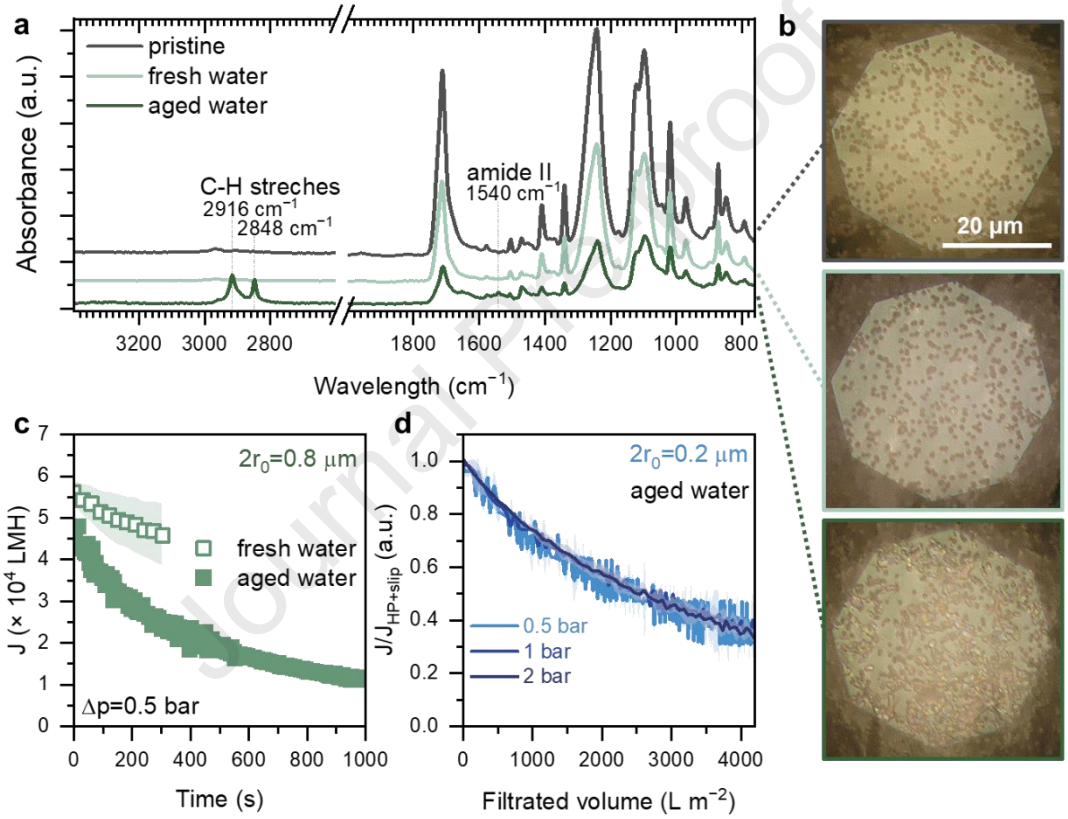

Figure 6. (a) ATR-FTIR spectra of pristine and post-filtrated with fresh and aged water TE-PET membrane ($2r_0$ = 0.8 µm, 20% porosity) (b) Optical microscope images of TE-PET membrane surface before and after filtration. (c) Water flux as a function of time of TE-PET membrane (0.8 µm pore at 0.5 bar) filtered with fresh and aged water. (d) Normalized flux decline with aged water for TE-PET membrane ($2r_0$ = 0.2 µm, 15.7% porosity) at different applied pressures plotted against filtrated volume.

Furthermore, the flux decline behaviour in fouled membranes was more closely related to the volume of water filtrated than to the filtration time (Figure 6d). When testing TE-PET membranes ($2r_0$ = 0.2 µm) with aged water, the flux decline curves at different applied pressures showed a single trend as a function of filtrated volume. This suggests that particle deposition followed by compaction of the fouling layer is the primary mechanism. In contrast, experiments with fresh

water showed divergent flux decline trends when plotted against filtrated volume (Figure S6) and exhibited minimal pressure dependence when plotted against time (Figure 2a), indicating that swelling is the dominant mechanism under normal operating conditions with clean water.

To quantitatively assess the flux decline behavior, Hermia's fouling model was applied to long-term cross-flow filtration data at 5 bar for TE-PET membranes with 1 µm pores and 0.3% porosity. The best fit was obtained for standard pore blocking mechanism, indicating that flux decline is governed by progressive pore restriction due to swelling during filtration. Fitting results are provided in the SI (Figure S7).

3.6 TE-PET as support for CNM-composite membranes

To evaluate the potential of TE-PET as a support material for advanced separation applications, we studied a novel thin film composite membrane, called CNM-composite with a carbon nanomembrane (CNM)[63–65] as active layer (Figure 7a) This is an ion-beamed (tracked) PET foil, coated on one side by a 20 nm aromatic based polymer film. This polymer film is cross-linked by low-energy electrons, thus forming a chemically and mechanically stable CNM active layer, which withstands the etching of the latent pores from the other side[46].

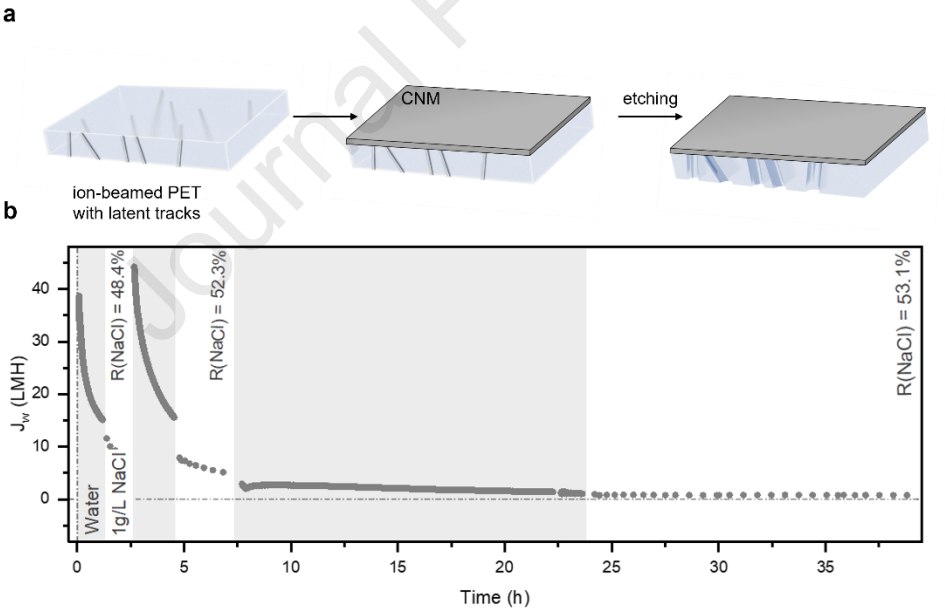

Figure 7. (a) Schematic presentation of CNM-composite fabrication method. (b) Water permeability and NaCl selectivity at 1 bar for CNM-composite membrane.

The water permeability and salt rejection characteristics of the CNM-composite membranes were evaluated through multiple filtration cycles in the LPRO setup (Figure 7b, solid line – pure water filtration, dotted line – 1 g/L NaCl filtration). The initial pure water flux of 40 LMH is two-order-of-magnitude lower compared to the bare TE-PET support (2 µm pores, 0.3% porosity with an initial

water flux of ~6000 LMH as calculated from Eq. 4), confirming the presence of additional CNM layer. The water permeability observed during the second measurement is higher compared to the first measurement which can be attributed to the insufficient wetting of the CNM layer during the initial filtration process. Under filtration with 1 g/L NaCl solution, the membrane achieved approximately 50% NaCl rejection, while maintaining its structural integrity. The observed performance, even when utilizing low-porosity (0.3%) TE-PET support, is comparable to that of the commercially available nanofiltration membrane NF270[66] However, similar to our observations with pristine TE-PET membranes, the composite structure exhibited progressive flux decline during operation. The maintained salt selectivity throughout testing suggests that the observed flux decline primarily originates from the support layer swelling rather than CNM layer degradation. This behaviour aligns well with the swelling-induced flux decline trends seen in the unmodified TE-PET membranes under similar operational conditions.

4. Conclusion

In this work, we demonstrated that water flux decline in TE-PET membranes originates from progressive swelling of the hydrophilic layer formed during chemical etching. The carboxyl and hydroxyl groups introduced upon pore formation promote water absorption and gel formation, leading to reduced effective pore diameters. This effect is particularly pronounced in larger pores, where geometric factors like reduced wall thickness and increased surface area accelerate the swelling process. We observed that 2.5 µm pores show flux decline within 70 seconds compared to 1200 seconds for 0.2 µm pores. When applied as supports for CNM-composite membranes, the resulting composite membrane showed promising initial performance with 40 $L/m^2 \cdot h \cdot bar$ water permeability (even at a porosity of the TE-PET support layer of only 0.3%) and 50% NaCl rejection, though long-term stability was limited by support layer swelling. Surface characterization confirmed significant morphological changes during filtration, while comparative solvent studies revealed that performance degradation is specific to water-membrane interactions.

The comprehensive characterization of TE-PET membranes and their behaviour in various filtration conditions reveals both challenges and opportunities for their application. While the swelling phenomenon presents a significant limitation for aqueous applications, our understanding of the underlying mechanisms, water absorption and volume expansion of residual oligomers containing carboxyl and hydroxyl groups within the ion tracks, provides clear directions of surface modification for future membrane development. The successful demonstration of CNM-composite membranes, despite the challenges posed by support layer swelling, indicates the potential of TE-PET as a platform for advanced separation technologies, particularly in organic solvent applications where the support shows excellent stability. These insights into structure-property relationships and performance limitations form the foundation for developing next-generation track-etched membranes with enhanced stability and broader application potentials.

5. Acknowledgements

This work is part of the FET Open project ITS-THIN funded by the European Union's Horizon 2020 research and innovation programme under grant agreement No. 899528. The authors acknowledge the use of Multiwin 3100 TOC/TNb analyzer (Analytic Jena GmbH, Jena, Germany), procured within the project "Upgrading national research infrastructures - RIUM", which was co-financed by the Republic of Slovenia, the Ministry of Higher Education, Science and Innovation and the European Union from the European Regional Development Fund. The authors sincerely appreciate R. Korzetz and M. Westphal for their contributions to HIM measurements, as well as to CNM Technologies GmbH for providing CNM-composite and TE-PET membranes.

6. Conflicts of interest

A.G. is the co-founder of CNM Technologies GmbH, a company focused on developing and marketing CNMs and CNM-composite membranes. P.A. is listed as an inventor on the international patent application WO 2019/228956 A1, titled "*Carbon Nanomembranes on Porous Materials*" as well as U.S. Patent US 10.646.831 B2 titled "*Method for manufacturing of a carbon nanomembrane*" (both assigned to CNM Technologies GmbH), which covers the manufacturing process of CNM-composite membranes. The other authors declare no conflicts of interest.

7. References

[1] P.Y. Apel, S.N. Dmitriev, Micro- and nanoporous materials produced using accelerated heavy ion beams, Advances in Natural Sciences: Nanoscience and Nanotechnology 2 (2011) 013002. https://doi.org/10.1088/2043-6262/2/1/013002.

[2] P.Y. Apel, Track etching technique in membrane technology, Radiat Meas 34 (2001) 559–566. https://doi.org/https://doi.org/10.1016/S1350-4487(01)00228-1.

[3] D. Fink, Fundamentals of Ion-Irradiated Polymers, Springer Science & Business Media, 2004.

[4] K.-J. Kim, P. V Stevens, A.G. Fane, Porosity dependence of pore entry shape in track-etched membranes by image analysis, J Memb Sci 93 (1994) 79–90. https://doi.org/https://doi.org/10.1016/0376-7388(94)85018-6.

[5] A. Popova, S. Boivin, T. Shintani, T. Fujioka, Development of high-integrity reverse osmosis membranes for enhanced removal of microorganisms, Desalination 572 (2024) 117155. https://doi.org/10.1016/j.desal.2023.117155.

[6] K.-J. Hwang, Y.-C. Chiang, Comparisons of membrane fouling and separation efficiency in protein/polysaccharide cross-flow microfiltration using membranes with different morphologies, Sep Purif Technol 125 (2014) 74–82. https://doi.org/https://doi.org/10.1016/j.seppur.2014.01.041.

[7] L. Zhu, W. Jia, M. Kattula, K. Ponnuru, E.P. Furlani, H. Lin, Effect of porous supports on the permeance of thin film composite membranes: Part I. Track-etched polycarbonate supports, J Memb Sci 514 (2016) 684–695. https://doi.org/10.1016/j.memsci.2015.11.043.

[8] S. Dutt, P.Y. Apel, N. Lizunov, C. Notthoff, Q. Wen, C. Trautmann, P. Mota-Santiago, N. Kirby, P. Kluth, Shape of nanopores in track-etched polycarbonate membranes, J Memb Sci 638 (2021) 119681. https://doi.org/10.1016/j.memsci.2021.119681.

[9] T.W. Cornelius, P.Y. Apel, B. Schiedt, C. Trautmann, M.E. Toimil-Molares, S. Karim, R. Neumann, Investigation of nanopore evolution in ion track-etched polycarbonate membranes, Nucl Instrum Methods Phys Res B 265 (2007) 553–557. https://doi.org/10.1016/j.nimb.2007.10.004.

[10] A. Delavari, D. Breite, A. Schulze, R.E. Baltus, Latex particle rejections from virgin and mixed charged surface polycarbonate track etched membranes, J Memb Sci 584 (2019) 110–119. https://doi.org/10.1016/j.memsci.2019.04.065.

[11] P.Y. Apel, I. V Blonskaya, V.R. Oganessian, O.L. Orelovitch, C. Trautmann, Morphology of latent and etched heavy ion tracks in radiation resistant polymers polyimide and poly(ethylene naphthalate), Nucl Instrum Methods Phys Res B 185 (2001) 216–221. https://doi.org/10.1016/s0168-583x(01)00967-3.

[12] K. Froehlich, M.C. Scheuerlein, M. Ali, S. Nasir, W. Ensinger, Enhancement of heavy ion track-etching in polyimide membranes with organic solvents, Nanotechnology 33 (2021) 045301. https://doi.org/10.1088/1361-6528/ac2f5a.

[13] K. Daumann, S. Frost, M. Ulbricht, Tunable and switchable nanoparticle separation with thermo-responsive track-etched membranes prepared by controlled surface-initiated polymerization of poly(N-isopropylacrylamide), RSC Adv 10 (2020) 21028–21038. https://doi.org/10.1039/d0ra03418e.

[14] A.A. Belkova, A.I. Sergeeva, P.Y. Apel, M.K. Beklemishev, Diffusion of aniline through a polyethylene terephthalate track-etched membrane, J Memb Sci 330 (2009) 145–155. https://doi.org/10.1016/j.memsci.2008.12.058.

[15] I.V Korolkov, A.A. Mashentseva, O. Güven, Y.G. Gorin, M. V Zdorovets, Protein fouling of modified microporous PET track-etched membranes, Radiation Physics and Chemistry 151 (2018) 141–148. https://doi.org/10.1016/j.radphyschem.2018.06.007.

[16] I.V Korolkov, O. Güven, A.A. Mashentseva, A.B. Atıcı, Y.G. Gorin, M. V Zdorovets, A.A. Taltenov, Radiation induced deposition of copper nanoparticles inside the nanochannels of poly(acrylic acid)-grafted poly(ethylene terephthalate) track-etched membranes, Radiation Physics and Chemistry 130 (2017) 480–487. https://doi.org/10.1016/j.radphyschem.2016.10.006.

[17] H. Hanot, E. Ferain, Industrial applications of ion track technology, Nucl Instrum Methods Phys Res B 267 (2009) 1019–1022. https://doi.org/10.1016/j.nimb.2009.02.011.

[18] H. Hanot, Use of High-Technology Track-Etched Polymer Membranes in a Wide Range of Industries, Am Biotechnol Lab 25 (2007) 24–26.

[19] P. Martínez-Pérez, J. García-Rupérez, Commercial polycarbonate track-etched membranes as substrates for low-cost optical sensors, Beilstein Journal of Nanotechnology 10 (2019) 677–683. https://doi.org/10.3762/BJNANO.10.67.

[20] K. Froehlich, S. Nasir, M. Ali, P. Ramirez, J. Cervera, S. Mafe, W. Ensinger, Fabrication of soft-etched nanoporous polyimide membranes for ionic conduction and discrimination, J Memb Sci 617 (2021) 118633. https://doi.org/10.1016/j.memsci.2020.118633.

[21] D. Kaya, K. Keçeci, Track-Etched Nanoporous Polymer Membranes as Sensors: A Review, J Electrochem Soc 167 (2020) 037543. https://doi.org/10.1149/1945-7111/ab67a7.

[22] S. Takahashi, M. Yoshida, M. Asano, T. Nakagawa, Gas-Permeation Control by PET Membranes with Nanosized Pores, Polym J 36 (2004) 50–53. https://doi.org/https://doi.org/10.1295/polymj.36.50.

[23] I.V. Korolkov, A.R. Narmukhamedova, G.B. Melnikova, I.B. Muslimova, A.B. Yeszhanov, Z.K. Zhatkanbayeva, S.A. Chizhik, M.V. Zdorovets, Preparation of Hydrophobic PET Track-Etched Membranes for Separation of Oil–Water Emulsion, Membranes (Basel) 11 (2021) 637. https://www.mdpi.com/2077-0375/11/8/637.

[24] I.B. Muslimova, Z.K. Zhatkanbayeva, D.D. Omertasov, G.B. Melnikova, A.B. Yeszhanov, O. Güven, S.A. Chizhik, M.V. Zdorovets, I.V. Korolkov, Stimuli-Responsive Track-Etched Membranes for Separation of Water–Oil Emulsions, Membranes 13 (2023) 523. https://doi.org/10.3390/membranes13050523.

[25] P.L.J. Lee, V. Thangavel, C. Guery, C. Trautmann, M.E. Toimil-Molares, M. Morcrette, Etched ion-track membranes as tailored separators in Li-S batteries, Nanotechnology 32 (2021) 365401. https://doi.org/10.1088/1361-6528/ac04a3.

[26] J. Liu, D. Cao, H. Yao, D. Liu, X. Zhang, Q. Zhang, L. Chen, S. Wu, Y. Sun, D. He, J. Liu, Hexagonal Boron Nitride-Coated Polyimide Ion Track Etched Separator with Enhanced Thermal Conductivity and High-Temperature Stability for Lithium-Ion Batteries, ACS Appl Energy Mater 5 (2022) 8639–8649. https://doi.org/10.1021/acsaem.2c01163.

[27] K. Cuanalo-Contreras, A.M.R. Hogrebe, K. Teichmann, D. Benkmann, Track-Etched Membranes for Drug Pharmaceutical Research, Chem Ing Tech 95 (2023) 1372–1380. https://doi.org/10.1002/cite.202300089.

[28] J. Zhao, Y. Zhang, Y. Su, J. Liu, X. Zhao, J. Peng, Z. Jiang, Cross-linked bovine serum albumin composite membranes prepared by interfacial polymerization with stimuli-response properties, J Memb Sci 445 (2013) 1–7. https://doi.org/10.1016/j.memsci.2013.05.050.

[29] L.E. Peng, Z. Yang, L. Long, S. Zhou, H. Guo, C.Y. Tang, A critical review on porous substrates of TFC polyamide membranes: Mechanisms, membrane performances, and future perspectives, J Memb Sci 641 (2022) 119871. https://doi.org/10.1016/j.memsci.2021.119871.

[30] A. Popova, T. Shintani, T. Fujioka, Track-etched membrane as a thin substrate with straight pores to fabricate polyamide forward osmosis membrane, Journal of Membrane Science Letters 4 (2024) 100068. https://doi.org/10.1016/j.memlet.2024.100068.

[31] L.E. Peng, Z. Yao, Z. Yang, H. Guo, C.Y. Tang, Dissecting the Role of Substrate on the Morphology and Separation Properties of Thin Film Composite Polyamide Membranes: Seeing Is Believing, Environ Sci Technol 54 (2020) 6978–6986. https://doi.org/10.1021/acs.est.0c01427.

[32] A. Popova, T. Shintani, T. Fujioka, Effects of substrate (track-etched filter) properties on the performance of forward osmosis membranes, J Memb Sci 704 (2024) 122865. https://doi.org/10.1016/j.memsci.2024.122865.

[33] S.N. Dmitriev, L.I. Kravets, V.V. Sleptsov, Modification of track membrane structure by plasma etching, Nuclear Instruments and Methods in Physics Research B 142 (1998) 43–49. https://doi.org/https://doi.org/10.1016/S0168-583X(98)00203-1.

[34] P.Y. Apel, I.V. Blonskaya, S.N. Dmitriev, T.I. Mamonova, O.L. Orelovitch, B. Sartowska, Y. Yamauchi, Surfactant-controlled etching of ion track nanopores and its practical applications in membrane technology, Radiat Meas 43 (2008) S552–S559. https://doi.org/10.1016/j.radmeas.2008.04.057.

[35] B.D. Tompkins, J.M. Dennison, E.R. Fisher, H2O plasma modification of track-etched polymer membranes for increased wettability and improved performance, J Memb Sci 428 (2013) 576–588. https://doi.org/10.1016/j.memsci.2012.10.037.

[36] K.B. Neeves, S.L. Diamond, A membrane-based microfluidic device for controlling the flux of platelet agonists into flowing blood, Lab Chip 8 (2008) 701–709. https://doi.org/10.1039/b717824g.

[37] M.R. Abror, S. Laksono, S. Adityosulindro, Comparative analysis of performance and fouling characteristics of microfiltration and ultrafiltration polycarbonate membrane, IOP Conf Ser Earth Environ Sci 1263 (2023) 012058. https://doi.org/10.1088/1755-1315/1263/1/012058.

[38] E.M. Tracey, R.H. Davis, Protein Fouling of Track-Etched Polycarbonate Microfiltration Membranes, J Colloid Interface Sci 167 (1994) 104–116. https://doi.org/https://doi.org/10.1006/jcis.1994.1338.

[39] P.Y. Apel, Y.E. Korchev, Z. Siwy, R. Spohr, M. Yoshida, Diode-like single-ion track membrane prepared by electro-stopping, Nuclear Instruments and Methods in Physics Research B 184 (2001) 337–346. https://doi.org/https://doi.org/10.1016/S0168-583X(01)00722-4.

[40] D.R. Lide, ed., CRC Handbook of Chemistry and Physics, 85th ed., American Chemical Society, 2005.

[41] V.A. Solanki, B. Borah, Ranking of Metal-Organic Frameworks (MOFs) for Separation of Hexane Isomers by Selective Adsorption, Ind Eng Chem Res 58 (2019) 20047–20065. https://doi.org/10.1021/acs.iecr.9b03533.

[42] K.I. Sawamura, T. Furuhata, Y. Sekine, E. Kikuchi, B. Subramanian, M. Matsukata, Zeolite Membrane for Dehydration of Isopropylalcohol-Water Mixture by Vapor Permeation, ACS Appl Mater Interfaces 7 (2015) 13728–13730. https://doi.org/10.1021/acsami.5b04085.

[43] Z. Song, Y. Huang, W.L. Xu, L. Wang, Y. Bao, S. Li, M. Yu, Continuously Adjustable, Molecular-Sieving “Gate” on 5A Zeolite for Distinguishing Small Organic Molecules by Size, Sci Rep 5 (2015) 5:13981. https://doi.org/10.1038/srep13981.

[44] L.R. Snyder, Classification of the solvent properties of common liquids, J Chromatogr Sci 16 (1974) 223–230. https://doi.org/https://doi.org/10.1016/S0021-9673(00)85732-5.

[45] M.E. Van Leeuwen, Derivation of Stockmayer potential parameters for polar fluids, Fluid Phase Equilib 99 (1994) 1–18. https://doi.org/https://doi.org/10.1016/0378-3812(94)80018-9.

[46] N. Meyerbröker, P. Angelova, A. Schnieders, H. Vieker, U.S. Patent, Carbon nanomembranes on porous materials, US 11666866B2, 2023.

[47] C.S. Ong, W.J. Lau, A.F. Ismail, Treatment of dyeing solution by NF membrane for decolorization and salt reduction, Desalination Water Treat 50 (2012) 245–253. https://doi.org/10.1080/19443994.2012.719473.

[48] F.F. Xu, Z.W. Liu, R. Huang, J.M. Zhang, J. Liu, Z.G. Hu, J. Ma, H.J. Yao, Y.M. Sun, Y.H. Chen, S.X. Zhang, D. Mo, J.L. Duan, Precisely Determined Water Permeabilities of Sub-100 nm Nanochannels, Adv Mater Interfaces 7 (2020) 2000307(1)-(7). https://doi.org/10.1002/admi.202000307.

[49] D. Fink, H.G. Muñoz, H. García A., J. Vacik, V. Hnatowicz, A. Kiv, L. Alfonta, Ion track etching revisited: I. Correlations between track parameters in aged polymers, Nucl Instrum Methods Phys Res B 420 (2018) 57–68. https://doi.org/10.1016/j.nimb.2018.02.009.

[50] A. Wolf, N. Reber, P.Y. Apel, B.E. Fischer, R. Spohr, Electrolyte transport in charged single ion track capillaries, Nuclear Instruments and Methods in Physics Research B 105 (1995) 291–293. https://doi.org/https://doi.org/10.1016/0168-583X(95)00577-3.

[51] D. Fink, Transport Processes in Ion-Irradiated Polymers, Springer Berlin Heidelberg, Berlin, Heidelberg, 2004. https://doi.org/10.1007/978-3-662-10608-2.

[52] T. Steckenreiter, E. Balanzat, H. Fuess, C. Trautmann, Chemical modifications of PET induced by swift heavy ions, Nuclear Instruments and Methods in Physics Research B 131 (1997) 159–166. https://doi.org/https://doi.org/10.1016/S0168-583X(97)00364-9.

[53] Z. Siwy, Y. Gu, H.A. Spohr, D. Baur, A. Wolf-Reber, R. Spohr, P.Y. Apel, Y.E. Korchev, Rectification and voltage gating of ion currents in a nanofabricated pore, Europhys Lett 60 (2002) 349–355. https://doi.org/10.1209/epl/i2002-00271-3.

[54] D.C. Grahame, Diffuse double layer theory for electrolytes of unsymmetrical valence types, J Chem Phys 21 (1953) 1054–1060. https://doi.org/10.1063/1.1699109.

[55] D.C. Grahame, The electrical double layer and the theory of electrocapillarity, Chem Rev 41 (1947) 441–501. https://doi.org/https://doi.org/10.1021/cr60130a002.

[56] T. Shigetomi, H. Tsuzumi, K. Toi, T. Ito, Sorption and diffusion of water vapor in poly(ethylene terephthalate) film, J Appl Polym Sci 76 (2000) 67–74. https://doi.org/https://doi.org/10.1002/(SICI)1097-4628(20000404)76:1<67::AID-APP9>3.0.CO;2-5.

[57] F. Dubelley, E. Planes, C. Bas, E. Pons, B. Yrieix, L. Flandin, Water Vapor Sorption Properties of Polyethylene Terephthalate over a Wide Range of Humidity and Temperature, Journal of Physical Chemistry B 121 (2017) 1953–1962. https://doi.org/10.1021/acs.jpcb.6b11700.

[58] S.K. Burgess, D.S. Mikkilineni, D.B. Yu, D.J. Kim, C.R. Mubarak, R.M. Kriegel, W.J. Koros, Water sorption in poly(ethylene furanoate) compared to poly(ethylene terephthalate). Part 1: Equilibrium sorption, Polymer (Guildf) 55 (2014) 6861–6869. https://doi.org/10.1016/j.polymer.2014.10.047.

[59] V.V. Berezkin, V.I. Volkov, O.A. Kiseleva, Electrosurface properties of poly(ethylene terephtalate) track membranes, Adv Colloid Interface Sci 104 (2003) 325–331. https://doi.org/10.1016/S0001-8686Ž03.00054-X.

[60] P. Déjardin, E.N. Vasina, V.V. Berezkin, V.D. Sobolev, V.I. Volkov, Streaming potential in cylindrical pores of poly(ethylene terephthalate) track-etched membranes: Variation of apparent ζ potential with pore radius, Langmuir 21 (2005) 4680–4685. https://doi.org/10.1021/la046913e.

[61] M.A. Vaz, J.C.R. Cyrino, G.G. da Silva, Three-Dimensional Stress Concentration Factor in Finite Width Plates with a Circular Hole, World Journal of Mechanics 03 (2013) 153–159. https://doi.org/10.4236/wjm.2013.33013.

[62] Y. Marcus, The properties of organic liquids that are relevant to their use as solvating solvents, Chem Soc Rev 22 (1993) 409–416. https://doi.org/10.1039/CS9932200409.

[63] W. Eck, A. Küller, M. Grunze, B. Völkel, A. Gölzhäuser, Freestanding Nanosheets from Crosslinked Biphenyl Self-Assembled Monolayers, Advanced Materials 17 (2005) 2583–2587. https://doi.org/10.1002/adma.200500900.

[64] A. Turchanin, A. Gölzhäuser, Carbon Nanomembranes, Advanced Materials 28 (2016) 6075–6103. https://doi.org/https://doi.org/10.1002/adma.201506058.

[65] P. Angelova, H. Vieker, N.-E. Weber, D. Matei, O. Reimer, I. Meier, S. Kurasch, J. Biskupek, D. Lorbach, K. Wunderlich, L. Chen, A. Terfort, M. Klapper, K. Müllen, U. Kaiser, A. Gölzhäuser, A. Turchanin, A Universal Scheme to Convert Aromatic Molecular Monolayers into Functional Carbon Nanomembranes, ACS Nano 7 (2013) 6489–6497. https://doi.org/10.1021/nn402652f.

[66] A. Ramdani, A. Deratani, S. Taleb, N. Drouiche, H. Lounici, Performance of NF90 and NF270 commercial nanofiltration membranes in the defluoridation of algerian brackish water, Desalination Water Treat 212 (2021) 286–296. https://doi.org/10.5004/dwt.2021.26680.

Highlights

- Sol-gel film swelling on pore walls causes water flux decline in TE-PET membranes.
- Larger pores (2.5 µm) show 80% flux reduction in 70 s vs. 1200 s for 0.2 µm pores.
- Swelling occurs only during filtration, not during static water immersion.
- Non-polar solvents like hexane show minimal flux decline compared to water.
- TE-PET supports show promise for composite membranes despite swelling limitations.

Declaration of interests

A.G. is the co-founder of CNM Technologies GmbH, a company focused on developing and marketing CNMs and CNM-composite membranes. P.A. is listed as an inventor on the international patent application WO 2019/228956 A1, titled "*Carbon Nanomembranes on Porous Materials*" as well as U.S. Patent US 10.646.831 B2 titled "*Method for manufacturing of a carbon nanomembrane*" (both assigned to CNM Technologies GmbH), which covers the manufacturing process of CNM-composite membranes. The other authors declare no conflicts of interest.